Journal for ImmunoTherapy of Cancer

Sensory neuron-derived CCL5 orchestrates an immunosuppressive niche via regulatory T cells to fuel head and neck tumor progression

Kailiu Wu,[1,2,3] Zhen Zhang,[1,2,3,4] Xing Qin,[1,2,3] Guanying Feng,[1,2,3] Huasheng Li,[1,2,3] Ruiyu Guo,[1,2,3] Yuhua Hu,[1,2,3] Yikang Ji,[1,2,3] Yang Wang,[5,6] Ming Yan ,[1,2,3] Chenping Zhang[1,2,3]

To cite: Wu K, Zhang Z, Qin X, *et al*. Sensory neuron-derived CCL5 orchestrates an immunosuppressive niche via regulatory T cells to fuel head and neck tumor progression. *Journal for ImmunoTherapy of Cancer* 2026;**14**:e013958. doi:10.1136/jitc-2025-013958

KW, ZZ and XQ contributed equally.

KW, ZZ and XQ are joint first authors.

Accepted 18 April 2026

For numbered affiliations see end of article.

Correspondence to
Prof. Yang Wang;
wangyang_zsyy@fudan.edu.cn

Prof. Ming Yan;
yanming8012@126.com

Prof. Chenping Zhang;
zhang.chenping@hotmail.com

ABSTRACT

Background Perineural invasion (PNI) is a hallmark of malignancy in solid tumors, including oral squamous cell carcinoma (OSCC), and is closely associated with poor prognosis. Emerging evidence suggests a critical association between PNI and the tumor immune microenvironment (TME).

Methods In this study, we used spatial transcriptomics, in vitro and in vivo experiments, and clinical specimen validation to systematically study the interplay between neural infiltration and immune modulation in OSCC.

Results Our results suggest that intratumoral nerves may enhance the recruitment of regulatory T cells (Tregs) through C-C motif chemokine ligand 5 (CCL5)-mediated chemotaxis and further promote the acquisition of an immunosuppressive phenotype in Tregs by activating the RAMP1 signaling pathway. Through these coordinated mechanisms, neural components in the TME contribute to immune suppression and facilitate tumor progression. Therapeutically, both combination of CCL5 blockade with anti-CTLA-4 antibody and the combination of RAMP1 blockade with anti-PD-1 antibody exhibited significantly enhanced anti-tumor efficacy.

Conclusions This study highlights a previously underappreciated neural-Treg axis in the TME and provides new insights into potential combinatorial strategies for cancer immunotherapy.

WHAT IS ALREADY KNOWN ON THIS TOPIC

⇒ Peripheral nerves contribute to tumor progression and immune regulation. Although neural interactions with tumor cells and immune subsets have been described, the role of Tregs in the neural niche of perineural invasion (PNI$^+$) tumors remains poorly understood.

WHAT THIS STUDY ADDS

⇒ This study provides evidence that sensory nerves promote a Treg-enriched immunosuppressive microenvironment and clarifies the mechanistic basis of neural-Treg interactions in head and neck cancer.

HOW THIS STUDY MIGHT AFFECT RESEARCH, PRACTICE OR POLICY

⇒ Targeting neural-Treg interactions may represent a potential approach to enhance immunotherapy efficacy in tumors with PNI.

INTRODUCTION

Oral squamous cell carcinoma (OSCC) is the most prevalent malignant tumor in the head and neck region, accounting for over 90% of head and neck cancers.[1 2] Patients often face challenges with chewing, speaking, and breathing postsurgery, and the 5-year survival rate is particularly low for those diagnosed at advanced stages. Risk factors for OSCC include tobacco and alcohol use, areca nut chewing, and poor oral hygiene, which contribute to chronic local inflammation induced by physical, chemical, or biological factors. Although studies have revealed numerous molecular events associated with OSCC, a thorough understanding of the spatial characteristics and interactions within the tumor microenvironment (TME) remains incomplete.

Besides the genome instability and mutations that occur during tumorigenesis and tumor-promoting inflammation from the microenvironment,[3] the interactions between the tumor and the nervous system are considered an important factor that promotes cancer cell growth and inhibits cytotoxic immune cells.[4] Numerous studies have revealed that the activities of the nervous system or neurons support the process of cancer in central nervous system-related tumors, including glioma,[5] by promoting proliferation and resistance to cell death. However, away from the central nervous system, the neural-related activities such as perineural invasions (PNIs) in other tumors were reported to interact with tumor and immune cells,[6] and multiple cancer cell types exhibited the potential to

hijack neural signals.[7] In fact, interactions in the peripheral neural-TME have been considered a candidate therapeutic target for cancer.[8] In OSCC, neurogenic calcitonin gene-related peptide (CGRP) is associated with poor prognosis and induces resistance to nutrient starvation therapies in OSCC.[9] However, research on the interactions between neural and immune microenvironments in OSCC remains limited.

Immune checkpoint blockade, an emerging immunotherapeutic strategy, has demonstrated unexpectedly promising efficacy in clinical trials for advanced OSCC; nevertheless, its therapeutic benefit is limited to approximately 15% of patients.[10] Tregs have been well known as the key effector to inhibit immune response and maintain immune tolerance.[11] In the cancer microenvironment, the cytotoxic effect of $CD8^+$T cells is depleted by Tregs through co-inhibitory signals via cytotoxic T-lymphocyte-associated protein 4 (CTLA-4) or through the secretion of inhibitory cytokines such as interleukin (IL)-10 and tumor growth factor (TGF)-β; therefore, Tregs are considered an optimal target for immune therapy.[12] However, the regulatory mechanisms of Treg function are highly complex and include a series of events involving transcription, post-translational modification, and metabolism.[13] Tumor evolution endows tumors with diverse strategies to modulate Treg function, including hypoxia, lactate, and others.[14] Signal from nociceptive nerves in the tumor was reported to mediate inhibitory microenvironment through macrophages[9] and T cells[15 16]; however, reports on regulating Tregs by nerves in the TME are scarce.

In this study, OSCC tissue samples with or without PNI were identified by pathological diagnosis and submitted for 10×Visium spatial transcriptomic sequencing. The cell composition and gene expression in the cancer area with or without nerve bundles were compared, and it was observed that the cancer area with PNI was infiltrated with more immune cells, and Tregs were the dominant cell lineage in the area, which promoted an inhibitory microenvironment. The ex vivo and in vivo study identified that the stimulation from nerves upregulated the expression levels of immune checkpoints in Tregs. The results of the cell–cell communication analysis suggested that CCL5 secreted by the neural niche recruits Tregs, subsequently activating the CGRP-RAMP1 axis. Tregs further reinforced the immunosuppressive TME, thereby promoting tumor progression. The mouse tumor-bearing model indicated that CCL5 and RAMP1 are candidate targets for combined therapy with immune checkpoint blockade in OSCC. To conclude, our study explored the spatial characteristics of PNI areas and proposed a novel immunotherapy strategy targeting neural invasion-related targets in OSCC, contributing to advancements in the potential cure of the disease.

MATERIALS AND METHODS

Sample collection

Fresh tumor tissues were obtained from patients with OSCC who underwent surgical resection at the Ninth People's Hospital. The inclusion criteria were as follows: (1) Histopathologically confirmed diagnosis; (2) no prior anti-tumor treatment before surgery; and (3) sufficient tissue available for analysis. Patients with recurrent tumors or incomplete clinical data were excluded from the study. A total of 60 tumor specimens were collected, including 17 females and 43 males, with ages ranging from 27 to 84 years. Among them, 30 were diagnosed with PNI, while the remaining 30 exhibited no evidence of PNI. All diagnoses were confirmed by experienced histopathologists. Written informed consent was obtained from all participants.

Sample preparation and data generation

For spatial transcriptomics, surgically resected tissues were placed in an OCT-filled mold and snap-frozen using isopentane and liquid nitrogen. Cryosections were stored at –80°C until further use. Between five and ten 5 µm-thick sections were prepared, and RNA was extracted using the RNeasy Mini Kit (#74104; Qiagen, Hilden, Germany) for immediate analysis. Samples with an RNA integrity number greater than seven were deemed suitable for analysis. The Visium Spatial Tissue Optimization slide was used to determine the optimal permeabilization conditions for tumor and normal tissues, following the 10×Visium spatial tissue optimization protocol. During cryosectioning, samples were equilibrated at –20°C, and tissue blocks were trimmed to dimensions smaller than 6.5×6.5 mm before being sectioned directly onto the optimization slide. The permeabilization time for the different tissue blocks ranged from 6 to 30 min. After establishing the optimal conditions, three cryosections per patient, each 10 µm thick, were mounted onto spatial slides and immediately processed.

The 10×Visium spatial gene expression protocol was strictly followed. The sectioned slides were stored at –20°C for 30 min. For staining, the slides were incubated sequentially with hematoxylin (#BCCC7207, SIGMA) for 10 min, bluing buffer (#091824, Dako) for 2 min, and eosin (#17372-87-1, Merck) diluted 1:9 in Tris-base for 1 min. Each staining step was followed by rinsing with RNase- and DNase-free water. Finally, the slides were imaged at 40× magnification using a microscope (Leica DMI8 and CS2).

The slides were placed in slide cassettes to partition the tissue sections into individual reaction chambers. The permeabilization enzyme from the 10×Visium Gene Expression Kit (PN-1000184) was applied to the tissue on the gene expression slide for the time determined during the tissue optimization step. Following incubation, the enzyme was removed, and the wells were rinsed with 0.1×SSC (#SLCF2892, SIGMA) before reverse transcription (RT) on a PCR instrument. After RT, the wells were washed again with 0.1×SSC. Subsequently, 75 µL of 0.08

M potassium hydroxide (KOH) was added to each well and incubated for 5 min at 25°C, after which the Second Strand Mix from the 10×Visium Gene Expression Kit (PN-1000184) was added to synthesize the second strand. Another 0.08 M KOH solution was added to each well for 10 min at 25°C. The cDNA yield was quantified using qPCR, and the double-stranded DNA was amplified by PCR based on the Cq values. Library preparation involved fragmentation, end repair, A-tailing, adapter ligation, and index PCR. The prepared libraries were sequenced using an Illumina NovaSeq platform. Data processing was performed using SpaceRanger (V.1.1.0; 10×Genomics, Pleasanton, California, USA), including the manual alignment of fiducial markers and manual identification of tissue boundaries.

Spatial transcriptomics data processing

Quality control results were obtained for all 18 527 spatial spots. The gene-spot matrices obtained from ST data processing of ST and Visium samples were analyzed using the 'Seurat' package (V.4.1.1) in R (V.4.1.0). Spot normalization was conducted with the 'SCTransform' function, and data from all four samples were integrated using the 'FindIntegrationAnchors' function. Dimensionality reduction and clustering were performed using principal component analysis (PCA) with the 'RunPCA' function. The cell proportion of each spot was calculated using the robust cell type decomposition (RCTD) method, and the reference single-cell RNA sequencing data were obtained from GSE200996.

Functional pathway enrichment analysis

ClusterProfiler[17] was used to perform gene set enrichment analysis (GSEA) and gene set variation analysis. Gene sets were obtained from the official GSEA database.[18 19] The enrichment results were integrated into the Seurat object and visualized using the SpatialFeaturePlot function to display their spatial distribution across tissue sections.

Single-cell data analysis

Seurat was used for preprocessing and analysis of the single-cell transcriptomic data. The unique molecular identifier (UMI) count matrix was processed using the Seurat R package, retaining genes expressed in more than three cells. Cells with fewer than 200 detected genes or with mitochondrial gene content exceeding 10% were excluded. PCA was performed on the 2000 most variable genes, and the top 25 principal components were subsequently used for dimensionality reduction with t-distributed stochastic neighbor embedding (t-SNE) and uniform manifold approximation and projection (UMAP) implemented using RunTSNE and RunUMAP functions in Seurat under default settings. Cell type annotation was conducted using SingleR [20] (V.1.8.1) and CellMarker (V.2.0).[21]

Visium spots annotation and nearest neighbors' analysis

RCTD[22] was applied to deconvolute the cellular composition of OSCC Visium spots. For spatial neighborhood estimation, the six nearest Visium spots were defined as spatial neighbors. Molecular and cellular neighborhood relationships were further identified using the Density-Based Spatial Clustering of Applications with Noise algorithm.[23]

Tumor boundary identification

Malignancy of spatial transcriptomics spots was assessed with Cottrazm.[24] Copy number variation (CNV) profiles were inferred using STInferCNV with non-malignant cell types as reference, and malignancy scores were calculated from CNV amplitudes (STCNVScore). Spots were further classified into malignant core (Mal), boundary (Bdy), and non-malignant (nMal) regions by BoundaryDefine for downstream analyses.

Spatial cell–cell communications

The Python package COMMOT[25] (COMMunication analysis by Optimal Transport) was used to infer cell–cell interactions from spatial transcriptomics data. Raw 10x Visium data were processed following the standard Scanpy workflow.[26] The CellChat database[27] was used to annotate ligand–receptor interactions and to perform spatial signaling stream analysis.

Bulk RNA-seq

Total RNA was extracted from cells using standard protocols, and RNA quality was assessed before library preparation. Sequencing libraries were constructed following the manufacturer's instructions and sequenced on an Illumina platform to generate paired-end reads. Raw reads were quality-controlled and aligned to the mouse reference genome (mm10). Gene expression levels were quantified, and differential expression analysis between groups was performed using DESeq2. Genes with an adjusted $p<0.05$ were considered significantly differentially expressed. Pathway enrichment analysis was conducted in R.

H&E staining and immunohistochemistry

Paraffin-embedded tissue sections (3 µm) were deparaffinized in xylene and rehydrated through graded ethanol. For H&E staining, sections were stained with H&E, dehydrated, cleared, and mounted. For immunohistochemistry (IHC), sections underwent heat-induced antigen retrieval in citrate buffer, followed by blocking of endogenous peroxidase with 0.3% hydrogen peroxide and non-specific binding with 3% goat serum albumin. Sections were incubated overnight at 4°C with primary antibodies against S100 (ORIGENE, ZM-0224, 1:100) and FOXP3 (ABCAM, ab20034; 1:200), followed by horseradish peroxidase-conjugated secondary antibody (Beyotime, A0208, 1:50) for 1 hour at room temperature. Nuclei were counterstained with hematoxylin, and slides were dehydrated, cleared, and mounted. Images were captured using a panoramic digital slide scanner (3D HISTECH, Hungary).

Multiple immunofluorescence staining and analysis

To prevent non-specific staining from antibodies of the same species, multiplex immunofluorescence staining was conducted using the TSA Plus kit, following the manufacturer's protocol for Tyramide Signal Amplification. After antigen retrieval, spontaneous fluorescence in the paraffin sections was eliminated using a tissue fluorescence quencher. All tissue sections were scanned using a Pannoramic Scanner, including the Pannoramic DESK, P-MIDI, and P250 models (3D HISTECH, Hungary), and the results were analyzed using ImageJ software.

Mouse trigeminal ganglion and Tregs co-culture models

The trigeminal ganglia (TGs) were dissected, rinsed with ice-cold phosphate-buffered saline (PBS) containing 4% penicillin/streptomycin, and preserved in neurobasal medium supplemented with B-27 and 4% penicillin/streptomycin. TGs were cultured for 1 week before experimentation, with half of the medium replaced every 2 days. Subsequently, half of the TGs were treated with 1 mM capsaicin (CAP) for three consecutive days and served as the control group. Following treatment, all TGs were washed thrice with PBS and cultured in 2.5 mL of Dulbecco's modified Eagle medium (DMEM) containing varying concentrations of glucose or glutamine for 72 hours. The conditioned medium (CM) was collected, centrifuged at 1500×g for 5 min, filtered through a 0.22 µm filter, and diluted 1:1.5 with fresh medium to ensure sufficient nutrients for the Tregs.

Transwell migration assay

A Transwell assay was performed to evaluate CCL5-induced migration of purified Tregs. Sorted Tregs were resuspended in serum-free medium and seeded into the upper chamber of Transwell inserts (5 µm pore size). The lower chamber contained (1) vehicle control, (2) recombinant CCL5, or (3) recombinant CCL5 plus a neutralizing anti-CCL5 antibody. After incubation at 37°C with 5% CO_2 for the indicated time, cells that migrated to the lower chamber were collected and counted. The number of migrated Tregs was compared among the groups. All experiments were performed in triplicate.

In vivo tumorigenicity assay

The mouse head and neck squamous cell carcinoma (HNSC) cell lines MOC1 and SCC7 were cultured in DMEM supplemented with 10% fetal bovine serum and 1% penicillin-streptomycin at 37°C in a humidified atmosphere containing 5% CO_2. Cells were passaged on reaching 80%–90% confluency.

C57BL/6 or C3H/HE mice aged 4–6 weeks were bought from Suzhou Cyagen Bioscience and housed in a specific pathogen-free environment for 1 week before experimentation. A total of 5×10^4 tumor cells mixed with Matrigel were injected into the submucosa of one side of the tongue. The mice were maintained for approximately 7 days before being randomly assigned to different treatment groups. Mice were treated with anti-CTLA-4 antibody (BioXcell, BE0164, 5 mg/kg, intraperitoneal injection, every 3 days), anti-CCL5 antibody (R&D, MAB478-500, 5 mg/kg, intraperitoneal injection, every 3 days), anti-PD-1 antibody (BioXcell, BE0146, 10 mg/kg, intraperitoneal injection, every 3 days), or rimegepant (MCE, HY-15498, 10 mg/kg, intraperitoneal injection, every day), as indicated. The mice were then subjected to the corresponding treatments and sacrificed at designated time points following the experimental design.

Flow cytometry

Samples from tissues or cultured cells were first processed into a single-cell suspension. The cells were washed with pre-cold PBS and stained with antibodies for 20 min. For intracellular staining, BD Cytofix/Cytoperm (BD Pharmingen, San Diego, California, USA) was used. The suspension was centrifuged for 5 min at 1000×g, and the cell pellet was resuspended in 400 µL PBS and evaluated using a flow cytometer. $CD45^+$ $CD3^+$ $CD8^+$ cells were used to gate $CD8^+$ T cells, and $CD45^+$ $CD3^+$ $CD4^+$ cells were used to gate $CD8^+$ T cells. Moreover, $CD45^+$ $CD3^+$ $CD4^+$ $CD25^+$ $Foxp3^+$ cells were used to gate Tregs. Besides, the expressions of RAMP1, CD274, PDCD1, and TIM3 were detected. Zombie Green Fixable Viability Kit was used to gate viable cells.

Statistical analysis and data visualization

All statistical analyses were conducted using R software (V.4.1.2). Differences in gene expression between the two groups were evaluated using the Wilcoxon rank-sum test, with statistical significance set at $p<0.05$. Data visualization was conducted using 'ggplot2' and 'ggsci' packages.

RESULTS

Spatial transcriptomics features of OSCC samples

Four OSCC samples were collected during surgery and submitted to 10X Visium spatial transcriptomics sequencing. Transcriptomics data of 18 527 spots were gained (figure 1), and reference single-cell sequencing data were analyzed and annotated in online supplemental figure S1A). Survival analysis based on The Cancer Genome Atlas (TCGA) HNSC data from 448 samples revealed that patients with PNI had a worse prognosis online supplemental figure S1B. H&E images of the four samples (TN0: without PNI; TN1-3 with PNI) are presented in figure 1B. The nerve tissue areas were labeled, and IHC staining results of S100 in three samples with PNI are presented in online supplemental figure S1C). Based on transcriptomic expression, the 18 527 spots were distributed into 23 clusters (figure 1C). Combining with the pathological diagnosis, the spots were further identified as neural niche, nerve-independent tumor, epithelial tissue, stroma, muscle, and immune cells enriched areas, as exhibited in figure 1D. The results revealed that the three samples with PNIs had larger nerve-related

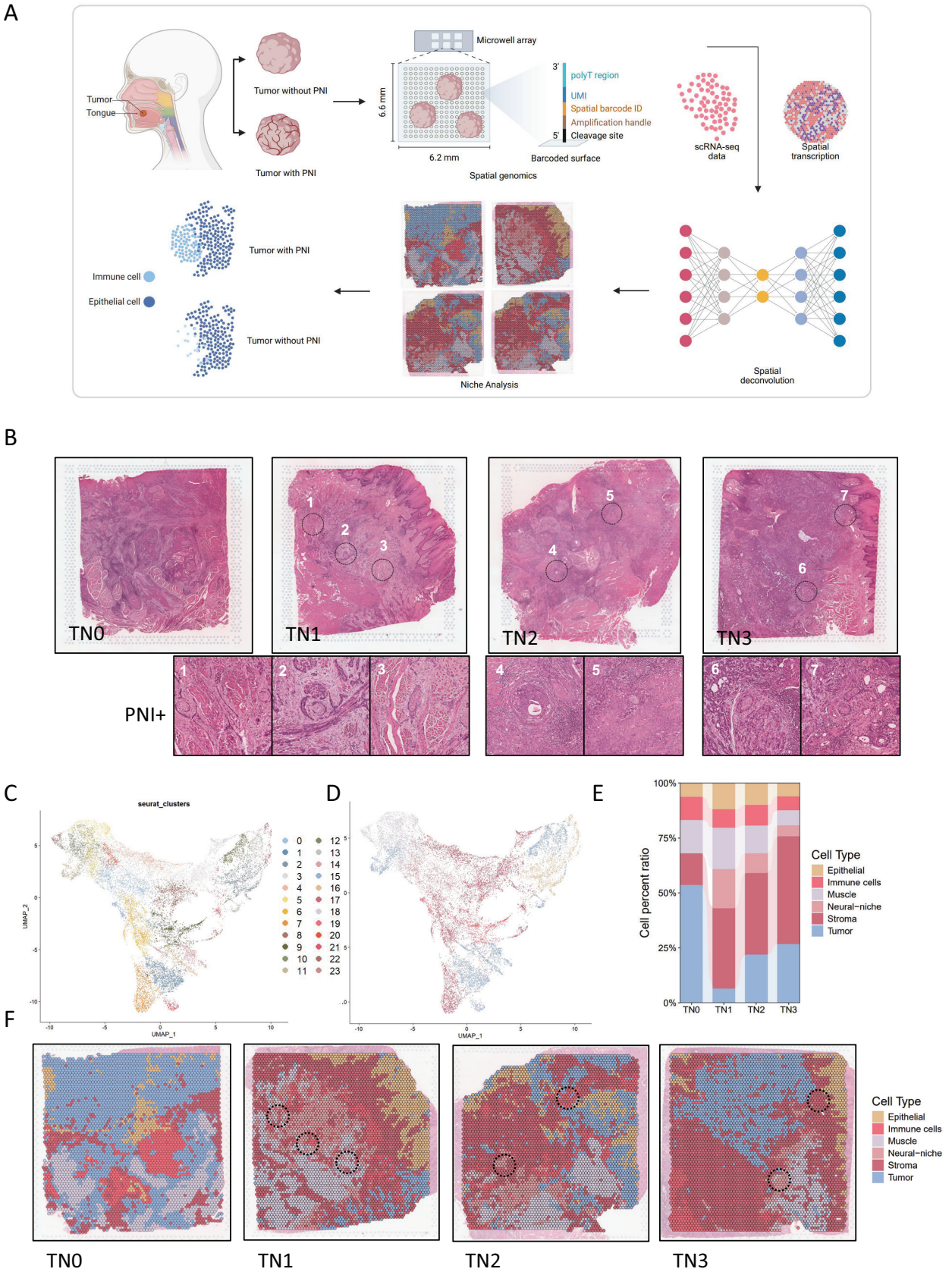

Figure 1 Spatial transcriptomics analysis of PNI samples. (A) OSCC sample spatial transcriptomics analysis flowchart; (B) H&E image of spatial transcriptomics samples with annotated nerve locations, TN0 is PNI– and TN1-3 are PNI+; (C) clustering of spatial transcriptomics spots; (D) annotation of spatial transcriptomics spots; (E) proportion of annotated spots in each sample; (F) spatial distribution of annotated spots. OSCC, oral squamous cell carcinoma; PNI, perineural invasion; TN0, tumor sample without PNI; TN1-3, tumor samples with PNI; UMI, unique molecular identifier.

tumor (neural niche) areas; however, the sample without PNIs had larger nerve-independent tumor areas (figure 1E). The spatial distribution of the different areas on samples with or without PNI is exhibited in figure 1F; the representative markers are presented in online supplemental figure S1D).

OSCC with or without PNI exhibited different oncogenesis mechanisms

The transcription levels of S100A and the sensory nerve marker TRPV1 were significantly higher in the neural niche area than in the tumor area (figure 2A). Commot was applied for signaling stream analysis in OSCC samples, and it was observed that the nerve growth factor (NGF) signaling pathway was only enriched in samples with PNI (figure 2B). Kyoto Encyclopedia of Genes and Genomes enrichment results for differentially expressed genes revealed that neural niche areas were more related to T cell differentiation and functions than the tumor area (figure 2C,D). Marker genes from the neural niche and tumor areas were also enriched using Metascape algorithm (online supplemental figure S2A) and GOBP terms (online supplemental figure S2B). Compared with tumor areas, marker genes in neural niche areas exhibited enrichment in a greater number of immune response-related pathways. We analyzed the copy number variations of the sample based on the infercnv algorithm (figure 2E and online supplemental figure S2C); the CNV level in the tumor area was significantly higher than that in the neural niche area. We then performed cell–cell interaction analysis using CellChat, and the results revealed that in the tumor area (figure 2F), the signals were more associated with the proliferation of tumor cells, including the EGF (Epidermal Growth Factor) signaling pathway network. However, in the neural niche areas (figure 2G), cytokines or chemokines, such as the TGFβ (Transforming Growth Factor-beta) signaling pathway, were more important. Further analysis of the EGF signaling pathway network (figure 2H), the TGFβ signaling pathway network (figure 2I), and the overall statistics of the interaction strength revealed that the neural niche area has more interactions with immune cells (figure 2G). These results indicate that although neural niche and tumor area were identified as malignant by pathologists, their inner drivers were different from each other, leading us to explore the relationship between PNI and the immune microenvironment.

PNI led to an inhibitory microenvironment by Treg infiltration

RCTD and cell neighbor methods were used to calculate the cell composition of each spot in the Visium sample. In samples with PNI, the neural niche areas were enriched with the most abundant immune cells (figure 3A,B), and Treg cells were the most dominant cell lineage among them (figure 3C). Visium data also revealed that Treg features were more abundant in the neural niche area than in the tumor area, and in the sample without PNI, there were fewer infiltrated Tregs (figure 3D). Then, we checked the expression levels of the immune checkpoint inhibitors (ICIs) genes and Treg markers on Visium data. The results revealed that *PDCD1, CTLA-4, TIGIT, HAVCR2, LAG3, FOXP3,* and *IL2RA* were mainly expressed in neural niche areas but not tumor areas (online supplemental figure S3A). Pathway analysis revealed that neural niche regions were characterized by enhanced metabolic activities, including glycolysis, oxidative phosphorylation, and fatty acid metabolism. Furthermore, inflammatory responses and cytokine production pathways were significantly enriched in these areas, whereas reactive oxygen species-related pathways were more prominently enriched in the tumor regions (online supplemental figure S3B). We adopted two gene signatures (anti-tumoral immunity and immunosuppression) from a recent study.[28] The overall activities of these two signatures were reflected in OSCC samples, revealing that anti-tumor immunity and immunosuppression were more enriched in the neural niche area; however, the immunosuppressive signals were more pronounced (online supplemental figure S3C).

We classified nerves into three categories: Peritumoral, intratumoral non-invaded, and intratumoral invaded. IHC results demonstrated that FOXP3 staining intensity increased progressively and significantly across the three groups (figure 3E). The differences in Treg cell percentage were analyzed in the presence or absence of PNI (figure 3F), depth of invasion (DOI) (figure 3G), and percentage of Tregs around nerve fascicles at different DOI levels (figure 3H). The results revealed that the percentage of Treg cells was significantly higher in tissue sections with PNI compared with those without. Moreover, the overall percentage of Tregs and the percentage of Tregs around nerve fascicles increased with greater DOI. To further assess whether Tregs were influenced by the PNI, immunofluorescence staining was performed to visualize the spatial distribution of nerves (PGP9.5 in yellow) and Tregs (FOXP3 in green). The tissue area was segmented based on the distance from nerve fascicles into three zones: <150 µm, 150–300 µm, and 300–450 µm (figure 4I). A progressive decrease in the number of $FOXP3^+$ cells was observed with increasing distance from the nerve fascicles, and this difference was statistically significant (figure 4J). Since Tregs were considered important anti-inflammation regulators in the TME, it was deduced that the interaction between nerves and Tregs was the main factor contributing to poor prognosis.

Neural niche region-derived CCL5 recruited Tregs to promote tumor growth

We further studied the mechanisms by which nerves might recruit Tregs and observed that the CCL signaling pathway may play an important role, particularly with a marked enhancement in the neural niche region compared with the tumor region alone (figure 4A and online supplemental figure S4A). Further analysis of the ligands and receptors involved in the CCL signaling pathway (figure 4B) revealed that CCL5 might be the most potent neural niche secreted ligand responsible for

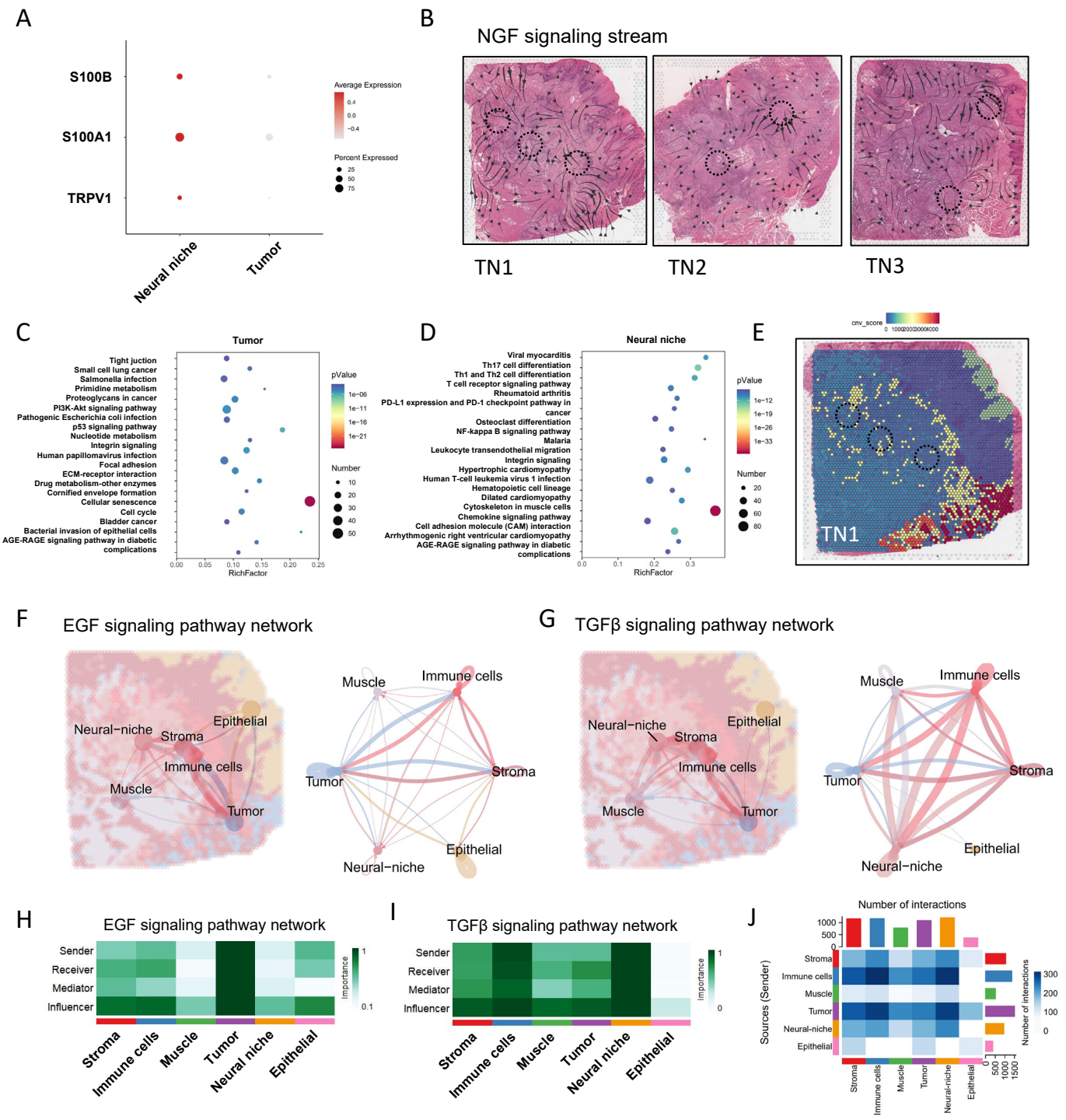

Figure 2 Comparison of molecular characteristics of the region between neural niche and tumor region without PNI. (A) Expression level of nerve-related markers from neural niche and tumor regions; (B) NGF (Nerve Growth Factor) signaling stream analysis by COMMOT algorithm in sample TN1-3; (C, D) KEGG enrichment of marker genes from tumor and neural niche regions; (E) spatial distribution of CNV scores of sample TN1; (F, G) spatial cell–cell interaction of the EGF signaling pathway network and TGFβ signaling pathway network by CellChat; (H, I) statistics of sender and receiver signal of EGF and TGFβ signaling pathways in annotated regions; (J) the total number of interaction strengths of different annotated regions. COMMOT, COMMunication analysis by Optimal Transport; CNV, copy number variation; KEGG, Kyoto Encyclopedia of Genes and Genomes; NGF, nerve growth factor; PNI, perineural invasion; EGF, Epidermal Growth Factor; TGFβ, Transforming Growth Factor-beta.

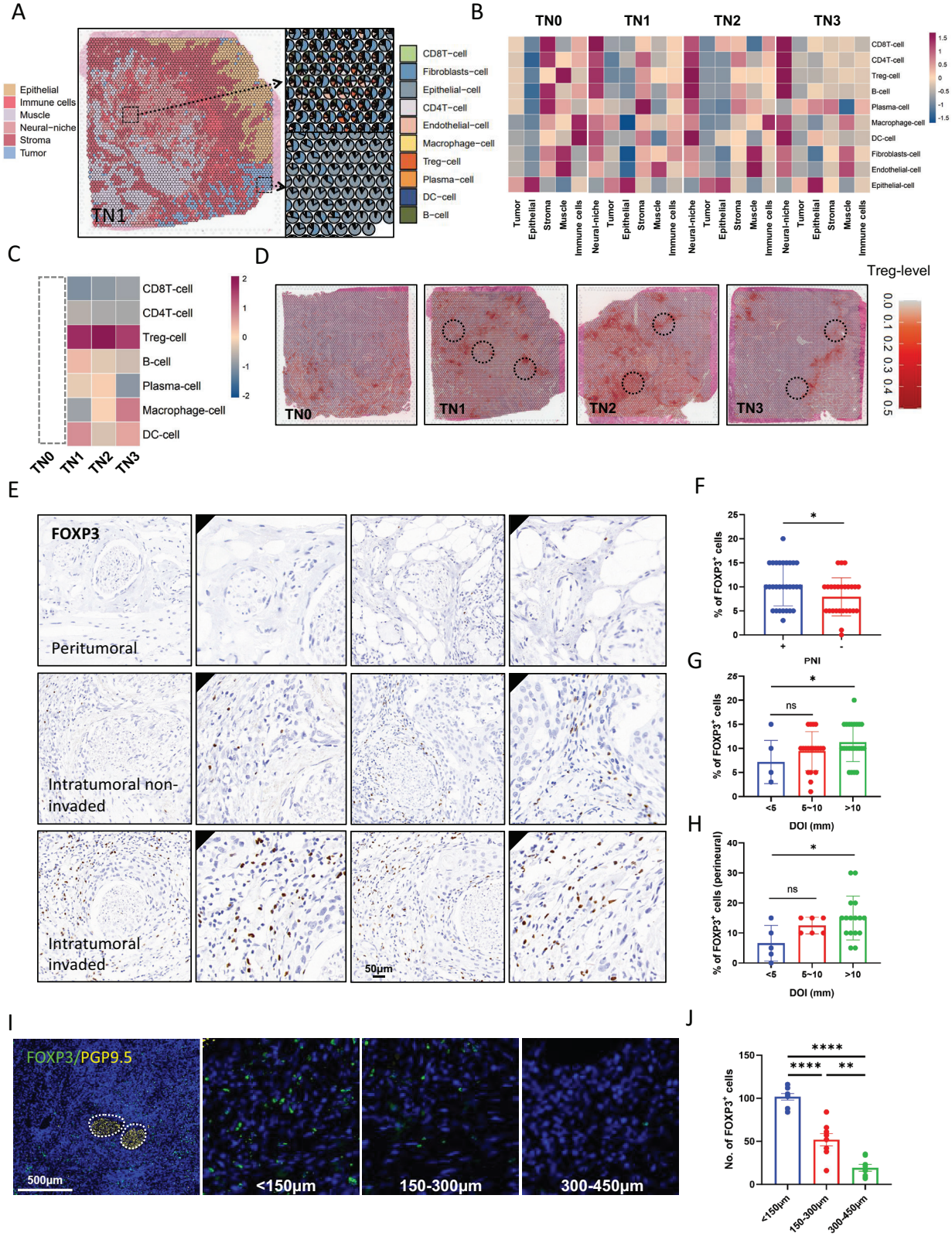

Figure 3 PNI promotes Treg infiltration. (A) Pie charts comparing cell-type composition between neural niche and tumor regions; (B, C) cell neighbor analysis of microenvironment cell composition of spatial transcriptomics data; (D) spatial distribution of Treg levels; (E) IHC of FOXP3 in peritumoral nerve, intratumoral non-invaded nerve, and intratumoral invaded nerve regions; (F) statistic of FOXP3$^+$ cells in sample with or without PNI; (G) statistic of FOXP3$^+$ cells in samples with different DOI; (H) statistic of perineural FOXP3$^+$ cells in samples with different DOI; (I) multiplex immunofluorescence exhibiting FOXP3 signal intensity in perineural regions; (J) statistic of FOXP3 signal intensity in perineural regions. DOI, depth of invasion; IHC, immunohistochemistry; PNI, perineural invasion; *P < 0.05, **P < 0.01, ***P < 0.001, ****P < 0.0001.

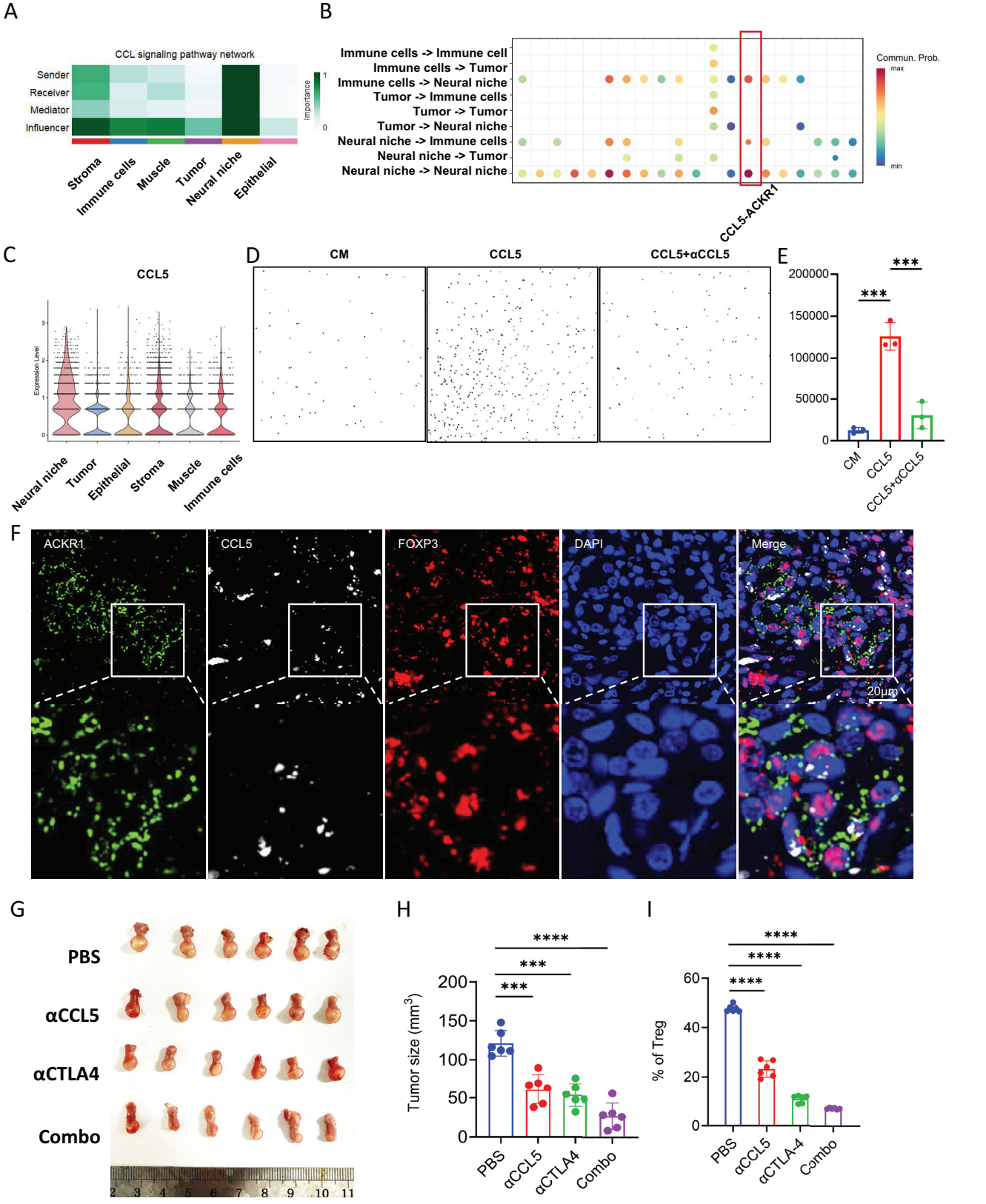

Figure 4 Tregs are recruited by the neural niche through CCL5. (A) Statistics of sender and receiver signal of CCL signaling pathways in annotated regions by cellchat; (B) analysis of ligand and receptor in CCL signaling pathway; (C) statistics of CCL5 levels in annotated regions of spatial transcriptomics data; (D) representative microscopic images from the Transwell migration assay validating the chemotactic effect of CCL5 on Tregs; (E) quantification of migrated Tregs in the Transwell assay; (F) immunofluorescence analysis exhibiting the colocalization of CCL5 and its receptor ACKR1; (G, H) tumor size in PBS, αCCL5, αCTLA-4, and combo groups; (I) flow cytometric analysis of Treg percentage. CM, Complete Medium; PBS, phosphate-buffered saline; *$P < 0.05$, **$P < 0.01$, ***$P < 0.001$, ****$P < 0.0001$.

Treg recruitment. Its spatial expression level is also significantly elevated in the neural niche region (figure 4C and online supplemental figure S4B); therefore, we speculate that the neural niche in the TME may recruit Tregs by promoting CCL5 secretion. The Transwell migration assay was used to validate the chemotaxis ability of CCL5 to Treg cells; the result revealed that CCL5 significantly promotes the Treg cell migration (figure 4D,E). CCL5 revealed high spatial colocalization with its receptor ACKR1 in the neural niche region (online supplemental figure S4C). The colocalization of ACKR1-CCL5 and ACKR1-Treg was validated by multiple immunofluorescence (mIF) result (figure 4F). Another mIF analysis further demonstrated that CCL5 was preferentially enriched near the sensory nerve marker CGRP, whereas its spatial association with fibroblast-related structures was limited. Notably, the macrophage marker CD68 was also highly enriched in the same region (online supplemental figure S4D). Taken together with the previous findings, these results suggest that sensory nerves within the neural niche region may enhance the local capacity for CCL5 production.

To further assess the anti-tumor efficacy of CCL5 blockade, we used a mouse orthotopic tongue cancer model. Tumor sizes were compared among the groups treated with the CCL5 antibody alone, CTLA-4 antibody alone, and a combination of both antibodies (online supplemental figure S4E). IHC results of PGP9.5 confirmed the presence of nerve tissue in the tumor (online supplemental figure S4F). Figure 4G reveals that treatment with CCL5 antibody alone significantly reduced tumor volume compared with the vehicle group. However, its efficacy was not superior to that of the CTLA-4 antibody alone. Notably, the combination of CCL5 and CTLA-4 antibodies exhibited greater tumor suppression than either treatment alone and significantly reduced the amount of Tregs, indicating a synergistic anti-tumor effect (figure 6H,I).

Nerves promoted the inhibitory function of Treg through the CGRP-RAMP1 axis

Visium data were screened with a series of nerve-derived ligands, and we observed that the RAMP1 signaling pathway is a potential contributor to the interactions between nerves and Tregs (figure 6A and online supplemental figure S5A). RAMP1 is the classic receptor of nerve-derived CGRP; its enrichment in PNI samples indicated the nerve-immune cell interactions in the TME. The colocalization of RAMP1 and Treg cells was validated with spatial transcriptomics data (figure 6B and online supplemental figure S5B). Figure 6C presents mIF staining results (FOXP3 in green, PGP9.5 in yellow, and CGRP in red) in a single field of view, comparing regions with and without PNI. Notably, the PNI-positive area exhibited much stronger FOXP3 and CGRP signals, whereas these signals were weak in the PNI-negative area. A line was drawn across PNI− and PNI+ regions within the field, and the fluorescence intensity along this line was quantified. The analysis revealed significantly higher FOXP3 and CGRP signals in the PNI+region (figure 6D).

RAMP1$^+$ Tregs were isolated from the total Treg population using flow cytometry. Compared with total Tregs, RAMP1$^+$ Tregs exhibited significantly elevated expression of immune checkpoint molecules, including TIM-3, PD-L1, and PD-1 (online supplemental figure S5C and D). To investigate the effect of nerves on Tregs, TG were extracted from mice and co-cultured with Tregs sorted from peripheral blood. The percentage of RAMP1$^+$ Tregs increased significantly after co-culture; however, this increase was abolished when CAP was added to inhibit the neural activity (figure 6E). We also assessed the mean fluorescence intensity (MFI) of immune checkpoint molecules and RAMP1. MFIs of RAMP1, FOXP3, CTLA-4, PD-1, and TIM-3 were enhanced following co-culture with TG but decreased when neural activity was suppressed by capsaicin (figure 6F–J). In an in vivo experiment using a mouse tongue tumor model (online supplemental figure S5E), CAP was injected subcutaneously into the suboccipital region to block the nerve function. The size and volume of the tumors in the CAP group were significantly lower than those in the vehicle group (figure 6K–M). However, the overall percentage of Tregs remained unchanged, and the proportion of RAMP1$^+$ Tregs in the Treg population decreased significantly following CAP treatment (figure 5N,O). Moreover, CAP treatment led to increased infiltration of CD8$^+$ T cells (figure 6P). To investigate the effect of blocking the CGRP-RAMP1 axis on Tregs, we redesigned an in vitro co-culture system and included the following treatment groups: vehicle, TG alone, CGRP alone, TG plus rimegepant, and CGRP plus rimegepant. The results revealed that RAMP1 expression and immune checkpoint levels were significantly upregulated under TG or CGRP stimulation. However, adding rimegepant effectively reversed these increases, suggesting that inhibition of the CGRP-RAMP1 axis attenuates Treg activation and immune checkpoint upregulation (figure 6Q–U). Using the GEPIA3 online tool, multivariate Cox regression analysis was performed based on TCGA-HNSC data. The results demonstrated that CGRP, compared with RAMP1, served as a more significant independent predictor of poor prognosis (online supplemental figure S5F).

Blockade of the CGRP-RAMP1 signaling axis alleviated the suppressive TME

In figure 5A, the spatial relationship between CD8$^+$ T cell Tregs was studied. In the neural niche regions, CD8$^+$ T cells were surrounded by Tregs.

The mIF results revealed that in cases with PNI, higher CGRP signals were associated with stronger FOXP3 signals and vice versa (figure 5B), indicating a positive correlation between CGRP expression and Treg infiltration. To clarify the intratumoral molecular events mediated by CGRP, T cells from mice treated with CGRP or CGRP plus rimegepant were subjected to RNA sequencing (figure 5C). Compared with the control group, CGRP

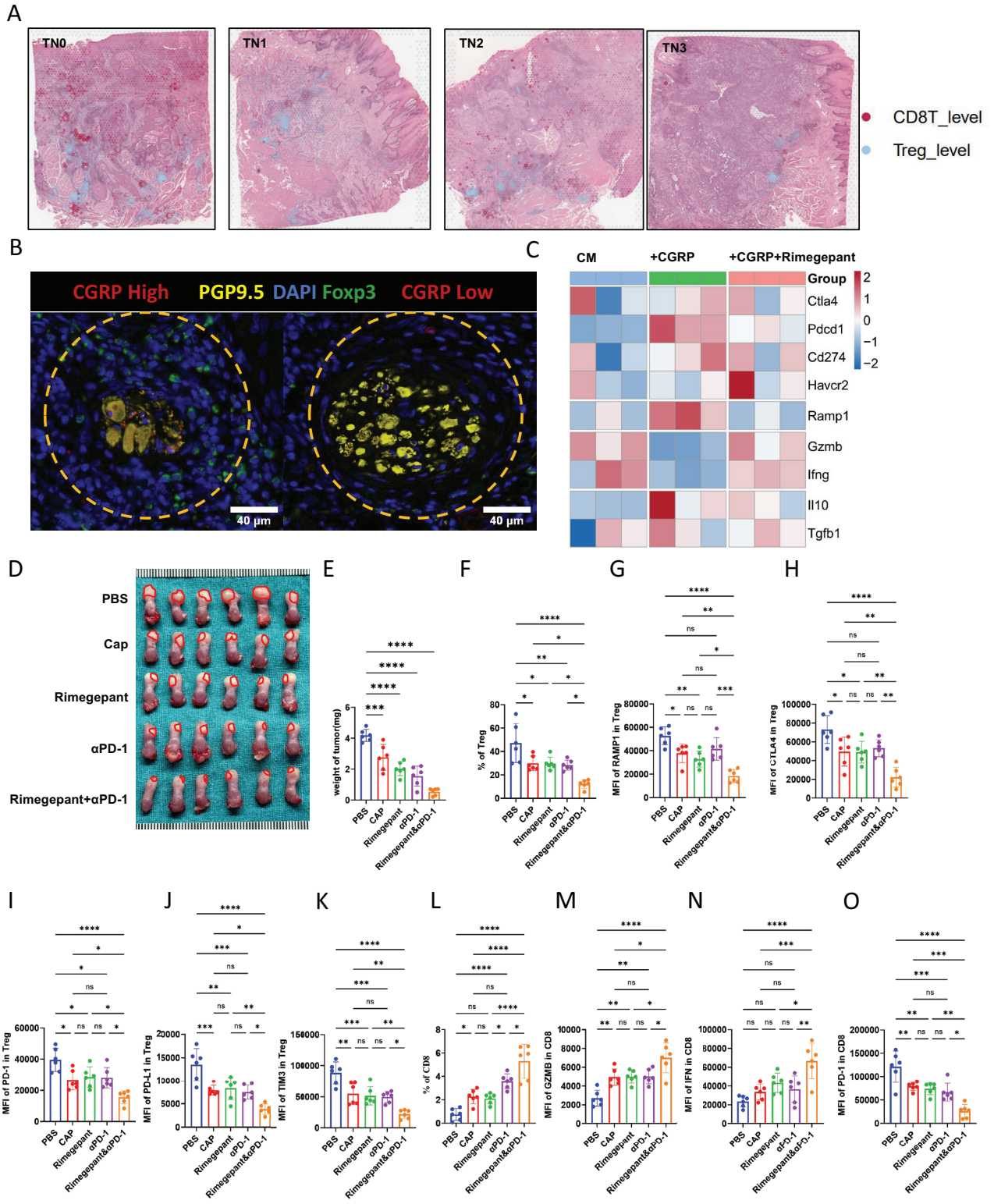

Figure 5 Effects of CGRP-RAMP1 axis blockade on TME. (A) Colocalization of Treg level and CD8T$^+$ cell level in spatial transcriptomics data; (B) MIF exhibiting FOXP3 signal intensity surrounding CGRP-high and CGRP-low nerve fibers; (C) RNA-seq analysis exhibiting changes in immune checkpoint molecules, Ramp1 expression, and pro- and anti-inflammatory cytokines in T cells treated with CGRP alone or CGRP plus rimegepant; (D) representative images of orthotopic tongue tumors from vehicle, CAP, rimegepant, anti-PD-1, and rimegepant plus anti-PD-1 treatment groups; (E) statistics of tumor weight of each group; (F) statistics of Treg percentage of each group; (G–K) statistics of levels of RAMP1 and ICIs of Tregs in each group; (L–O) statistics of cell percentage, levels of GZMB, levels of IFN, and levels of PD-1 of CD8$^+$ T cells in each group. CAP, capsaicin; CGRP, calcitonin gene-related peptide; CM, conditioned medium; ICIs, immune checkpoint inhibitors; MFI, mean fluorescence intensity; mIF, multiple immunofluorescence; PBS, phosphate-buffered saline; TME, tumor microenvironment; $^*P < 0.05$, $^{**}P < 0.01$, $^{***}P < 0.001$, $^{****}P < 0.0001$.

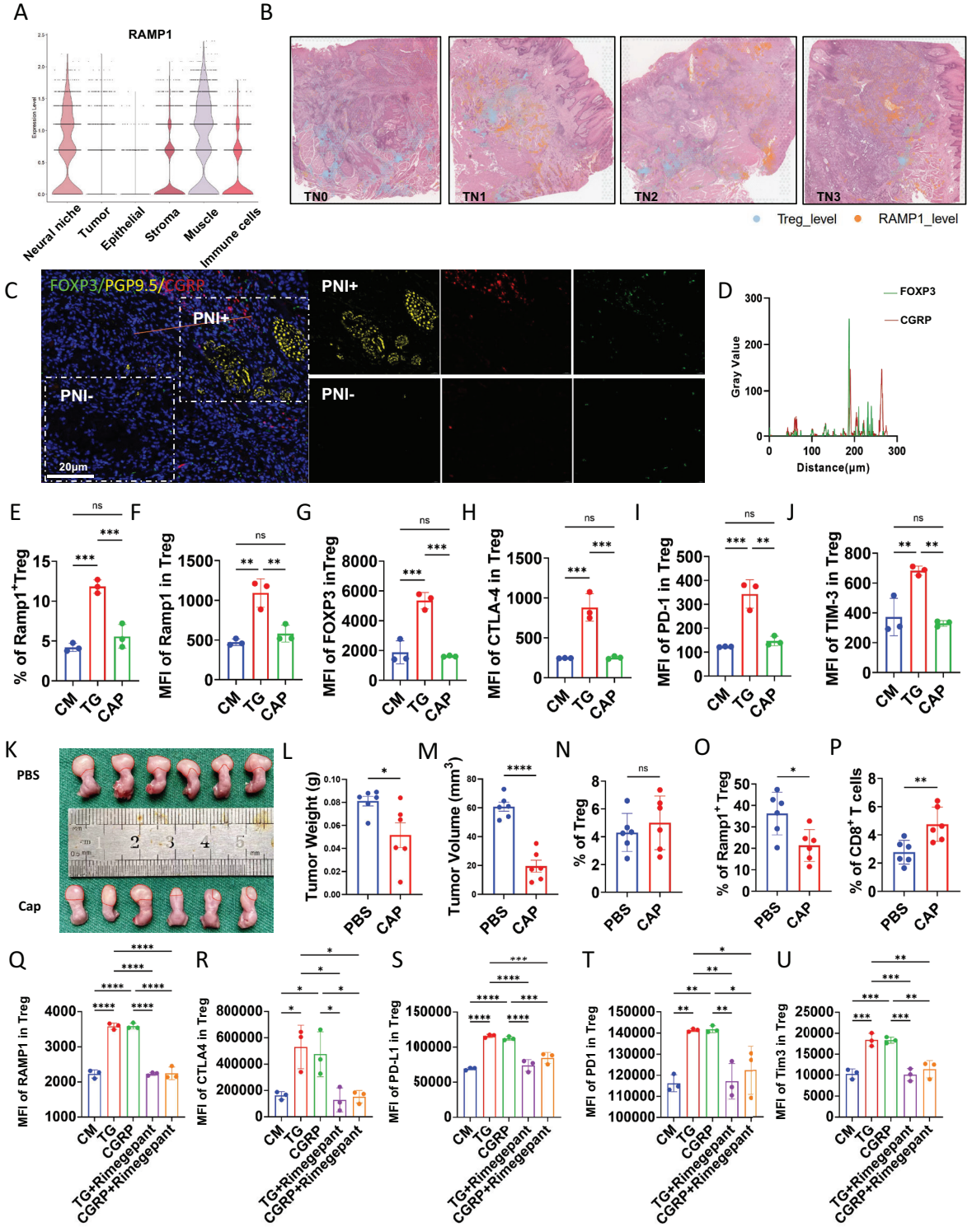

Figure 6 Inhibitory phenotypes of Treg are promoted by the CGRP-RAMP1 axis in the neural niche. (A) Expression level of RAMP1 in annotated regions of spatial transcriptomics data; (B) colocalization of Treg level and RAMP1 level in spatial transcriptomics data; (C) multiplex immunofluorescence exhibiting the distribution of FOXP3 and CGRP signals in PNI$^+$ and PNI$^-$ regions; (D) colocalization of FOXP3 and CGRP signals from mIF result; (E) statistics of RAMP1$^+$ Treg percentage of CM, TG, and CAP groups; (F–J) statistics of MFI of RAMP1 level and ICI levels in Tregs from CM, TG, and CAP groups; (K) representative images of orthotopic tongue tumors in PBS-treated and CAP-treated mice; (L, M) tumor weight and size comparison in vehicle and CAP groups; (N–P) statistics of Treg percentage, RAMP1$^+$ Treg percentage, and CD8$^+$ T cell percentage; (Q–U) in vitro co-culture analysis of CGRP-RAMP1 signaling in Tregs. Tregs were treated with vehicle, TG alone, CGRP alone, TG plus rimegepant, or CGRP plus rimegepant, and RAMP1 expression and immune checkpoint levels were assessed. CAP, capsaicin; CM, conditioned medium; MFI, mean fluorescence intensity; mIF, multiple immunofluorescence; PBS, phosphate-buffered saline; PNI, perineural invasion; TG, trigeminal ganglia; *P < 0.05, **P < 0.01, ***P < 0.001, ****P < 0.0001.

treatment significantly upregulated the expression of immune checkpoint molecules, *Ramp1*, and the canonical immunosuppressive cytokines of Tregs, *Il10,* and *Tgfb1*. Conversely, the cytotoxic effector molecule *Gzmb* and *Ifng* in $CD8^+$ T cells were markedly downregulated. Notably, these alterations were partially reversed in the CGRP plus rimegepant group. Differential gene enrichment analysis further revealed that CGRP treatment activated multiple immune-related pathways, consistent with our previous findings (online supplemental figure S6A). We designed an in vivo experiment to evaluate the therapeutic efficacy of CGRP-RAMP1 blockade in combination with an anti-PD-1 antibody (online supplemental figure S6B). The results revealed that CAP treatment, rimegepant monotherapy, and anti-PD-1 monotherapy significantly reduced tumor growth, whereas the combination of rimegepant and anti-PD-1 therapy achieved the most pronounced anti-tumor effect (figure 6D,E). From the perspective of Tregs, the combination therapy markedly decreased Treg infiltration, reduced RAMP1 expression, and lowered the levels of multiple ICI molecules (figure 5F–K). Conversely, regarding $CD8^+$ T cells, combination therapy significantly increased $CD8^+$ T cell infiltration and enhanced the expression of cytotoxic markers GZMB and IFN-γ, whereas PD-1 expression was significantly reduced (figure 5L–O). These findings suggest a synergistic effect of CGRP-RAMP1 blockade and PD-1 inhibition in remodeling the tumor immune microenvironment.

DISCUSSION

Pain is suggested to be the initial symptom of oral cancer and is reported to be a common complaint in patients both pretreatment and post-treatment.[29] Pretreatment pain is a signal of poor pathological features, including PNI and lymph node metastasis in OSCC. Immune modulation of the microenvironment affects cancer progression and pain signaling, indicating the important role of nerve tissue in cancer development.[30] Tumor-associated nerves induce local inflammation and promote resistance to anti-PD-1 therapy. The results revealed that non-responders had higher rates of PNI, nerve damage, and degeneration, together with more infiltration of M2 macrophages and Tregs.[31] Neuroinflammation, mitochondrial dysfunction, and cellular metabolism were also observed in OSCC.[32] Although the prognostic value of PNI remains debated, emerging evidence indicates its role in promoting head and neck cancer.[33] In this study, our evidence depicted that PNI is associated with the poor prognosis of patients with OSCC, and the depth of tumor invasion has the greatest impact on PNI.

Recently, there has been a growing number of studies reporting on the mechanisms underlying the regulation of the neural and immune microenvironments in tumors. Among the studies, CGRP derived from nociceptive neurons is most well studied; the CGRP and neural growth factor in gastric tumors stimulate the cancer cell growth.[34] NGF secretion from cancer-associated fibroblasts promotes the invasion of neural tissue around the invasion margin and further accelerates CRC proliferation.[35] The neural and matrix interactions also inhibit the function of natural killer cells in PDAC.[36] In head and neck cancer, neurogenic CGRP induces cytoprotective autophagy in cancer cells.[9] T cells are important members of the TME, and their activities are also affected by CGRP. For example, the CGRP-RAMP1 signal promotes the T helper type 1 differentiation to increase the antiviral function.[15] Conversely, the interaction between CGRP and RAMP1 receptor on $CD8^+$ T leads to the upregulation of PD-1 and CTLA-4, affecting cancer immunosurveillance.[16] In our study, Tregs were recruited to the PNI region, and the levels of RAMP1 and immune checkpoint molecules increased after co-culture with nerve tissue, establishing a relationship between nerves and Tregs. The enhanced expression of RAMP1 and immune checkpoint molecules observed in PNI^+ regions may reflect intensified neuroimmune interactions within the neural niche microenvironment.[37] In the context of PNI, sensory neurons release neuropeptides, including CGRP, which signals through the CGRP receptor complex containing RAMP1. Increased RAMP1 expression may sensitize immune cells to CGRP-mediated signaling, thereby amplifying downstream cAMP-dependent pathways.[38] Such activation may promote an immunosuppressive phenotype characterized by Treg recruitment and functional stabilization, accompanied by increased expression of immune checkpoint molecules, including PD-1 and CTLA-4. Additionally, CGRP signaling may indirectly enhance checkpoint expression by upregulating immunoregulatory cytokines, including IL-10 and TGF-β.[39] Together, these findings suggest that neural signaling in PNI^+ regions contributes to the reinforcement of immune checkpoint activation and immune evasion.

The feasibility of targeting the interactions between peripheral nerves and the tumor immune microenvironment as a therapeutic strategy is increasingly being recognized, particularly by disrupting the connections between nerves and immune cells or nerves and tumor cells.[8] Potential targets include adrenergic signaling,[40] GABA,[41] acetylcholine,[42] dopamine,[43] and CGRP signaling.[9] Blockade of tumor-associated neural activities impairs the tumor's survival capacity by inhibiting the tumor growth signaling, altering its metabolism status, and reversing the immunosuppressive microenvironment. In this study, we designed two combination immunotherapy strategies targeting distinct mechanisms within the neural niche. The first combined a neutralizing anti-CCL5 antibody with anti-CTLA-4 to inhibit Treg recruitment and enhance $CD8^+$ T cell activation. The second approach targeted the CGRP–RAMP1 axis by combining rimegepant with anti-PD-1 to suppress Treg function and restore anti-tumor immunity. Both regimens revealed significant therapeutic efficacy. Notably, rimegepant plus anti-PD-1 achieved significant anti-tumor effects and was also associated with a reduction in Treg infiltration. Given that

anti-CTLA-4 therapy is associated with a higher risk of immune-related adverse events affecting major organs such as the heart, liver, lungs, kidneys, and gastrointestinal tract due to the disruption of immune tolerance, the combination of rimegepant and anti-PD-1 may represent a safer and effective therapeutic strategy.[44 45]

With advances in single-cell RNA sequencing and spatial transcriptomics, we can elucidate the differences in the TME between oral cancers with and without PNI. However, neuronal cells are relatively difficult to capture during single-cell RNA sequencing, making it challenging to directly visualize neurons in spatial transcriptomics data. Future research may leverage high-resolution spatial transcriptomics to enable finer characterization of tumor tissue structures and deeper investigation into the underlying biological mechanisms. In summary, our findings demonstrate that PNI facilitates the formation of an immunosuppressive microenvironment through its impact on Tregs, thereby providing a theoretical and experimental foundation for future investigations.

Author affiliations
[1]Department of Oral and Maxillofacial-Head and Neck Oncology, Shanghai Ninth People's Hospital, Shanghai Jiao Tong University School of Medicine, Shanghai, China
[2]College of Stomatology, Shanghai Jiao Tong University, Shanghai, China
[3]National Center for Stomatology; National Clinical Research Center for Oral Diseases; Shanghai Key Laboratory of Stomatology; Shanghai Research Institute of Stomatology; Shanghai Center of Head and Neck Oncology Clinical and Translational Science, Shanghai, China
[4]Digital Diagnosis and Treatment Innovation Center for Cancer, Institute of Translational Medicine, Shanghai Jiao Tong University, Shanghai, China
[5]Department of Oral and Maxillofacial Surgery, Zhongshan Hospital, Fudan University, Shanghai, China
[6]Fengcheng Hospital of Fengxian District, Shanghai, China

Acknowledgements The flowchart was produced by BioRender and the graphical abstract was produced by Figdraw.We thank Home for Researchers editorial team (www.home-for-researchers.com) for language editing service.

Contributors CZ, MY, and YW designed the project. KW, ZZ, and XQ performed the experiments, data statistics, and bioinformatics analysis. GF provided support during animal experiments and data visualization. HL, RG, and YJ kindly provided support in cytologic assays. YH provided support in pathological analysis of clinical samples. KW and ZZ wrote the manuscript. All the authors read and approved the final manuscript. CZ is the guarantor of this work, responsible for the overall content and ensuring the integrity of the research. During the preparation of this work, the authors used ChatGPT in order to improve the language and clarity of the manuscript. After using this tool/service, the authors reviewed and edited the content as needed and take full responsibility for the content of the publication.

Funding This work was supported by grants from the National Natural Science Foundation of China (82373352 and 82173217) by MY; the National Natural Science Foundation of China (82472922) and Natural Science Foundation of Shanghai (21ZR1453900) by YW; the National Natural Science Foundation of China (82002935) and Shanghai Sailing Program (20YF1424100) by XQ; the Explorers Program of Shanghai (Basic Research Funding) (25TS1403702) by ZZ and Shanghai Shenkang Hospital Development Center Project (SHDC2020CR3008A) by CZ.

Competing interests No, there are no competing interests.

Patient consent for publication Not applicable.

Ethics approval The study was approved by the Ethics Committee of the Ninth People's Hospital, Shanghai Jiao Tong University School of Medicine (Approval No.: SH9H-2025-T323-1). Participants gave informed consent to participate in the study before taking part. All animal procedures were performed in accordance with the guidelines and regulations of the Laboratory Animal Ethics Committee in Ninth People's Hospital Affiliated to Shanghai Jiao Tong University School of Medicine (Approval No. SH9H-2025-A1609-1). Every effort was made to minimize animal suffering and to reduce the number of animals used.

Provenance and peer review Not commissioned; externally peer reviewed.

Data availability statement Data are available in a public, open access repository. Data are available on reasonable request. Data are available on reasonable request. In: OMIX, National Genomics Data Center (NGDC), accession OMIX015304. Available: https://ngdc.cncb.ac.cn/omix/release/OMIX015304

ORCID iD
Ming Yan https://orcid.org/0000-0002-7126-5976

REFERENCES

1 Ren ZH, Hu CY, He HR, *et al*. Global and regional burdens of oral cancer from 1990 to 2017: Results from the global burden of disease study. *Cancer Commun (Lond)* 2020;40:81–92.
2 Siegel RL, Miller KD, Fuchs HE, *et al*. Cancer statistics, 2022. *CA Cancer J Clin* 2022;72:7–33.
3 Hanahan D, Weinberg RA. Hallmarks of cancer: the next generation. *Cell* 2011;144:646–74.
4 Hanahan D, Monje M. Cancer hallmarks intersect with neuroscience in the tumor microenvironment. *Cancer Cell* 2023;41:573–80.
5 Venkatesh HS, Johung TB, Caretti V, *et al*. Neuronal Activity Promotes Glioma Growth through Neuroligin-3 Secretion. *Cell* 2015;161:803–16.
6 Guo X, Pan Y, Xiong M, *et al*. Midkine activation of $CD8^+$ T cells establishes a neuron-immune-cancer axis responsible for low-grade glioma growth. *Nat Commun* 2020;11:2177.
7 Xu Q, Cao Y, Kong F, *et al*. Multiple cancer cell types release LIF and Gal3 to hijack neural signals. *Cell Res* 2024;34:345–54.
8 Yaniv D, Mattson B, Talbot S, *et al*. Targeting the peripheral neural-tumour microenvironment for cancer therapy. *Nat Rev Drug Discov* 2024;23:780–96.
9 Zhang Y, Lin C, Liu Z, *et al*. Cancer cells co-opt nociceptive nerves to thrive in nutrient-poor environments and upon nutrient-starvation therapies. *Cell Metab* 2022;34:1999–2017.
10 Burtness B, Harrington KJ, Greil R, *et al*. Pembrolizumab alone or with chemotherapy versus cetuximab with chemotherapy for recurrent or metastatic squamous cell carcinoma of the head and neck (KEYNOTE-048): a randomised, open-label, phase 3 study. *Lancet* 2019;394:1915–28.
11 Huppert LA, Green MD, Kim L, *et al*. Tissue-specific Tregs in cancer metastasis: opportunities for precision immunotherapy. *Cell Mol Immunol* 2022;19:33–45.
12 Tay C, Tanaka A, Sakaguchi S. Tumor-infiltrating regulatory T cells as targets of cancer immunotherapy. *Cancer Cell* 2023;41:450–65.
13 Montauti E, Weinberg SE, Chu P, *et al*. A deubiquitination module essential for T_{reg} fitness in the tumor microenvironment. *Sci Adv* 2022;8:eabo4116.
14 Liu Z, Zhang Z, Zhang Y, *et al*. Spatial transcriptomics reveals that metabolic characteristics define the tumor immunosuppression microenvironment via iCAF transformation in oral squamous cell carcinoma. *Int J Oral Sci* 2024;16:9.
15 Hou Y, Sun L, LaFleur MW, *et al*. Neuropeptide signalling orchestrates T cell differentiation. *Nature New Biol* 2024;635:444–52.
16 Balood M, *et al*. Nociceptor neurons affect cancer immunosurveillance. *Nature New Biol* 2022;611:405–12.
17 Xu S, Hu E, Cai Y, *et al*. Using clusterProfiler to characterize multiomics data. *Nat Protoc* 2024;19:3292–320.

18 Mootha VK, *et al*. PGC-1α-responsive genes involved in oxidative phosphorylation are coordinately downregulated in human diabetes. *Nat Genet* 2003;34:267–73.
19 Subramanian A, Tamayo P, Mootha VK, *et al*. Gene set enrichment analysis: a knowledge-based approach for interpreting genome-wide expression profiles. *Proc Natl Acad Sci U S A* 2005;102:15545–50.
20 Aran D, *et al*. Reference-based analysis of lung single-cell sequencing reveals a transitional profibrotic macrophage. *Nat Immunol* 2019;20:163–72.
21 Hu C, Li T, Xu Y, *et al*. CellMarker 2.0: an updated database of manually curated cell markers in human/mouse and web tools based on scRNA-seq data. *Nucleic Acids Res* 2023;51:D870–6.
22 Cable DM, Murray E, Zou LS, *et al*. Robust decomposition of cell type mixtures in spatial transcriptomics. *Nat Biotechnol* 2022;40:517–26.
23 Hahsler M, Piekenbrock M, Doran D dbscan. Fast Density-Based Clustering with R. *J Stat Softw* 2019.
24 Xun Z, Ding X, Zhang Y, *et al*. Reconstruction of the tumor spatial microenvironment along the malignant-boundary-nonmalignant axis. *Nat Commun* 2023;14:933.
25 Cang Z, Zhao Y, Almet AA, *et al*. Screening cell-cell communication in spatial transcriptomics via collective optimal transport. *Nat Methods* 2023;20:218–28.
26 Wolf FA, Angerer P, Theis FJ. SCANPY: large-scale single-cell gene expression data analysis. *Genome Biol* 2018;19:15.
27 Jin S, Guerrero-Juarez CF, Zhang L, *et al*. Inference and analysis of cell-cell communication using CellChat. *Nat Commun* 2021;12:1088.
28 Baruch EN, Gleber-Netto FO, Nagarajan P, *et al*. Cancer-induced nerve injury promotes resistance to anti-PD-1 therapy. *Nature New Biol* 2025;646:462–73.
29 Dios PD, Lestón JS. Oral cancer pain. *Oral Oncol* 2010;46:448–51.
30 Ye Y, Jensen DD, Viet CT, *et al*. Advances in Head and Neck Cancer Pain. *J Dent Res* 2022;101:1025–33.
31 Baruch EN, Nagarajan P, Gleber-Netto FO, *et al*. Inflammation induced by tumor-associated nerves promotes resistance to anti-PD-1 therapy in cancer patients and is targetable by interleukin-6 blockade. *Res Sq* 2023.
32 Zhang M, Yuan M, Asam K, *et al*. Perineural Invasion Exhibits Traits of Neurodegeneration. *J Dent Res* 2025;104:1352–60.
33 Rutkowski K, Gola M, Godlewski J, *et al*. Understanding the role of nerves in head and neck cancers - a review. *Oncol Rev* 2024;18:1514004.
34 Zhi X, Wu F, Qian J, *et al*. Nociceptive neurons promote gastric tumour progression via a CGRP-RAMP1 axis. *Nature New Biol* 2025;640:802–10.
35 Kobayashi H, Iida T, Ochiai Y, *et al*. Neuro-Mesenchymal Interaction Mediated by a β2-Adrenergic Nerve Growth Factor Feedforward Loop Promotes Colorectal Cancer Progression. *Cancer Discov* 2025;15:202–26.
36 Wang K, Ni B, Xie Y, *et al*. Nociceptor neurons promote PDAC progression and cancer pain by interaction with cancer-associated fibroblasts and suppression of natural killer cells. *Cell Res* 2025;35:362–80.
37 Zhang Y, Guo Y, Liu Z, *et al*. Cancer cells co-opt an inter-organ neuroimmune circuit to escape immune surveillance. *Cell* 2025;188:6754–73.
38 Wu M, Song G, Li J, *et al*. Innervation of nociceptor neurons in the spleen promotes germinal center responses and humoral immunity. *Cell* 2024;187:2935–51.
39 Volobueva MN, Suleymanova EM, Smirnova MP, *et al*. A Single Episode of Cortical Spreading Depolarization Increases mRNA Levels of Proinflammatory Cytokines, Calcitonin Gene-Related Peptide and Pannexin-1 Channels in the Cerebral Cortex. *Int J Mol Sci* 2022;24:85.
40 Wang HM, Liao ZX, Komaki R, *et al*. Improved survival outcomes with the incidental use of beta-blockers among patients with non-small-cell lung cancer treated with definitive radiation therapy. *Ann Oncol* 2013;24:1312–9.
41 Zhang X, Du Z, Liu J, *et al*. Γ-aminobutyric acid receptors affect the progression and migration of tumor cells. *J Recept Signal Transduct Res* 2014;34:431–9.
42 Chen J, Cheuk IWY, Shin VY, *et al*. Acetylcholine receptors: Key players in cancer development. *Surg Oncol* 2019;31:46–53.
43 Grant CE, Flis AL, Ryan BM. Understanding the role of dopamine in cancer: past, present and future. *Carcinogenesis* 2022;43:517–27.
44 Martins F, Sofiya L, Sykiotis GP, *et al*. Adverse effects of immune-checkpoint inhibitors: epidemiology, management and surveillance. *Nat Rev Clin Oncol* 2019;16:563–80.
45 Skoulidis F, Araujo HA, Do MT, *et al*. CTLA4 blockade abrogates KEAP1/STK11-related resistance to PD-(L)1 inhibitors. *Nature New Biol* 2024;635:462–71.